Thermo-luminescent optical fibre sensor for Li-ion cell internal temperature monitoring

Elise Villemin, Sylvie Genies, Olivier Poncelet, Pierre Balfet, Cédric Septet, Romain Franchi, Martin Guillon, Jérôme Houny, Sonia Sousa-Nobre, Olivier Raccurt

Preprint version

Thermo-luminescent optical fibre sensor for Li-ion cell internal temperature monitoring

Elise Villemin[1], Sylvie Genies[1], Olivier Poncelet[2], Pierre Balfet[1], Cédric Septet[1], Romain Franchi[1], Martin Guillon[1], Jérôme Houny[1], Sonia Sousa-Nobre[2], Olivier Raccurt[1*]

[1] Univ. Grenoble Alpes, CEA, LITEN, DEHT, F-38000 Grenoble, France
[2] Univ. Grenoble Alpes, CEA, LITEN, DTNM, F-38000 Grenoble, France

* Corresponding author: olivier.raccurt@cea.fr

Abstract

The internal temperature of a Li-ion battery is one of the critical parameters for monitoring cell performance, ageing and safety. The development of new sensor technologies to control the internal temperature of cells without compromising performance and safety remains a challenge. It is one of the objectives of the European INSTABAT project in the framework of the Battery2030+ initiative. The objective of this paper is to describe the development of a new optical fibre sensor based on a thermoluminescent material to monitor internal cell temperature. The development of the sensor, its thermal characterisation and its calibration are presented here. This sensor was inserted into a commercial Li-ion cell and its response during cycling at high charge and discharge rates (2C in charge and 4C in discharge) was investigated. The comparison between external and internal temperature measurements shows good agreement. These results demonstrate the ability of this type of sensor to monitor the internal temperature of a Li-ion battery without affecting its performance at high loading.

Keywords: Li-ion batteries; Optical Fibre; Temperature Sensors; Fast-charging; *operando* analysis, Smart-cell

Abbreviations

B_i : The Biot number, B: Constant in expression of *FIR*, CCD: Charge-Coupled Device,δT: Temperature uncertainty (K), ΔE: Energy difference between two barycentre of the coupled level (radiative transition) using for calculation of *FIR,* F: $^2F_{9/2}$ to $^4I_{15/2}$ radiative transition, *FIR*: Fluorescence Intensity Ratio, h: Global thermal transfer coefficient (0.5 W/m/K), H: $^2H_{11/2}$ to $^4I_{15/2}$ radiative transition, I_{cell}: Cell current (I), I_i (i=1 or 2) Luminescence intensity of the two peaks 1 and 2 use for FIR calculation, IR: Infrared, k_B:Boltzmann constant, λ_b: Thermal conductivity (0.5W/m/K), L_c: Characteristic length in our case the half of cell thickness (1 mm), LED: Light Emissive Diode, NIR: Near Infrared, PMMA: Poly Methyl Methacrylate, S: $^4S_{3/2}$ to $^4I_{15/2}$ radiative transition, S_a:Absolute sensitivity, S_r: Relative Sensitivity, SOC: State of Charge, T: Temperature (K), T_{ext}:External temperature of the cell (K), T_{int}: Internal temperature of the cell (K), U_{cell}: Cell potential (V), UV: Ultraviolet, VIS: Visible light, QY= Quantum Yield

Graphical abstract

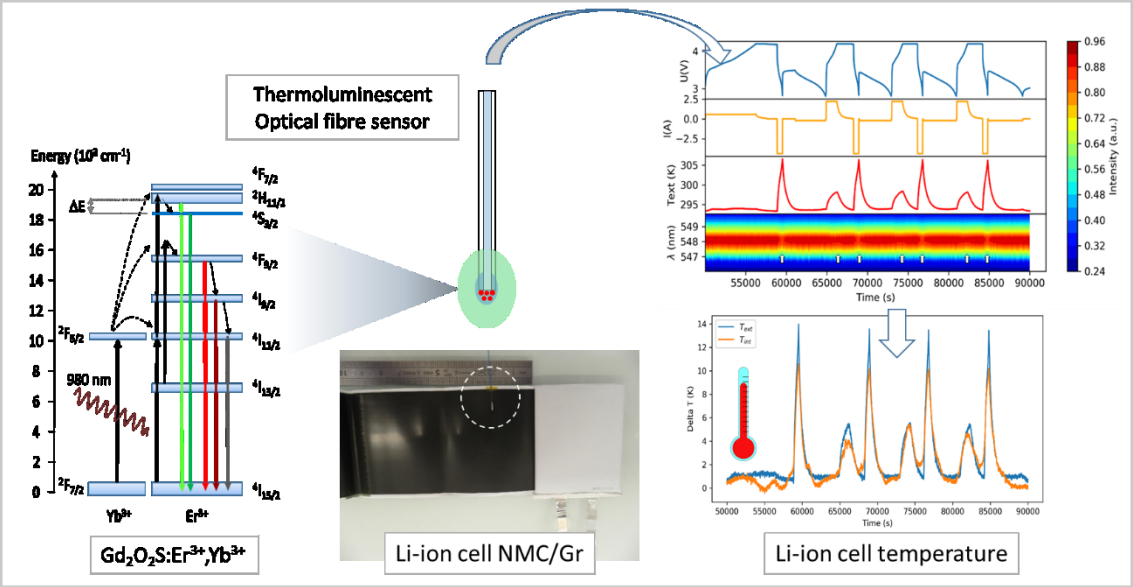

1. Introduction

Improving battery safety and performance requires developing battery management systems with accurate estimators (state of charge, state of health, state of safety, etc.) based on monitoring critical cell parameters in real-time [1]. The measurement of internal cell parameters should provide better understanding of degradation mechanisms, failure prevention and ageing anticipation. To achieve these goals, the development of new sensor technologies is required and their integration inside Li-ion batteries without affecting cell performance and safety remains challenging [2,3]. These goals are clearly identified in the roadmap of the Battery2030+ initiative [4] and are currently pursued by three European projects on smart batteries: INSTABAT, SENSIBAT and SPARTACUS [5]. Among the important physical parameters, the internal temperature of the cell is one of the most critical since the temperature determines performance, ageing and safety [6]. Much effort must be devoted to cell and pack design to limit temperature increases and to develop accurate and non-invasive techniques to measure the internal temperature of the cell [7]. Measuring the internal temperature of the cell raises problems. Thermal sensors must be compatible with the chemistry of the cell and small in size. In addition, the insertion of thermal sensors must not affect the performance, ageing or safety of the cell. Among the different sensor technologies, optical fibre sensors have been developed [8,9] due to their fast response, their compact size, which allows their integration in multiple environments, and their immunity to electromagnetic fields. This kind of sensor has already proved its worth in monitoring the internal parameters of Li-ion cells [10–22].

Fibre Bragg Gratings (FBG) sensors are widely used to monitor the internal and external temperature of the cell. This technique has several advantages such as the possibility of having several sensors in the same fibre, high sensitivity and good accuracy. However, the signal response of FBG sensors is dependent on temperature and strain, and it is difficult to properly decouple these two contributions [23–27]. One solution is the use of two optical fibres to decouple temperature and strain. However, sensor integration increases the complexity and size of the sensor, which can affect the correct operation of the cell. Recent

work by J. Pinto *et al.* [28] reported a new strategy to decouple temperature and strain measurement with the same optical fibre by using panda fibre with FBG sensors. Another publication from J.M. Tarascon's team [27] obtained results from the comparison of two types of optical fibres with FBG sensors to decouple strain and temperature. However, this kind of FBG sensor requires an expensive interrogator which makes it difficult to integrate this sensor into a BMS while managing performance, cost and size.

Using thermoluminescent probes is another way of measuring temperature using optical fibre. This technique was developed a long time ago for various applications [29–32]. Phosphor co-doped with trivalent lanthanide ions has been selected from the thermoluminophore family due to its long-term thermoluminescence properties (no or low photobleaching and fast and reproducible response) and its chemical and thermic stability over time [29,32]. Some examples present temperature sensors based on optical fibres incorporating phosphor doped with trivalent cations. However, these temperature sensors are either limited for their temperature range and not really designed for specific applications [33–37] (development of materials and the corresponding temperature sensors as proofs of concept), or they are compatible only with a specific environment such as in photonic applications [36,38]. The luminescence of inorganic materials used for thermoluminescent probe depends only on temperature and is completely independent of the surrounding chemical environment and strain [29,32]. The measurement can be performed by using low-cost light sources and a portable spectrophotometer [32,39]. This detection system is cheaper than commercial FBG interrogators and can be easily used for *in-situ* measurements (*e.g.,* in vehicle battery packs). There are many techniques for measuring temperature with luminescence [39]. The ratiometry technique is based on the relative intensity variation of two radiative transitions. This technique presents a few advantages from the others such as relative independence from the excitation sources and easier detection with cheaper components compared to the lifetime based method [40]. A temperature sensor dedicated to *in situ* temperature monitoring requires a temperature range between 253 K to 423 K corresponding to the operating range of Li-ion battery temperature (with optimal use in the restricted temperature zone of 293 to 313 K). This particular temperature range differs from the classical ranges used in the development of temperature sensors for other applications (such as biological applications with the temperature range around the physiological temperature [41] and industrial applications with high temperature ranges [29]). Furthermore, the development of sensors for Li-ion batteries must meet additional prerequisites: such as a mechanical resistance due to their integration inside the battery (for *in-situ* temperature monitoring) as well as a chemical resistance to the battery environment and particularly to the by-products resulting from the lithium salts formed during the electrochemical cycling of the battery [42]. Despite the fact that this type of sensor has been used in many fields for several years, to our knowledge only one article mentions its application for measuring the internal temperature of a battery [43]. In this paper, H. Li *et al.* used β-$NaYF_4$:Er^{3+}/Yb^{3+}@$NaYF_4$ nanoparticles embedded in a PMMA matrix deposit at the end of an optical fibre to monitor the internal temperature of a pouch cell (NMC111/Graphite, 3.7V, 1200 mAh. They demonstrated the capability of a thermoluminescent optical fibre sensor to monitor the internal temperature of the cell. However, these thermoluminescent nanoparticles have low efficiency (*i.e.* quantum yield in upconversion) and consequently require the use of a high-power laser source for excitation. However, for industrial applications, such as battery management systems, it is crucial to reduce the cost and size of the sensor.

In this study, we demonstrate the possibility of using a more efficient thermoluminescent optical fibre sensor, based on one of the most efficient commercial upconverter materials, and associated with a low-cost excitation source such as a Light Emissive Diode (LED). The choice of excitation wavelength and its

potential negative effect on the cell components is another parameter to consider. Some thermoluminophores require UV excitation. However, UV light could damage the organic materials inside the cell such as the separator and the electrode binder. Moreover, UV light requires more expensive optics than visible (VIS) and near-infrared (NIR) light. For these reasons, we focus our work on an inorganic material excited by near-infrared (NIR) light (980 nm) with luminescence emission in the visible wavelength range (between 400 to 700 nm). Herein, we present the performance and the potential of a new temperature sensor based on optical fibre dedicated to Li-ion battery internal temperature *operando* monitoring. First, the temperature dependency of the luminescence of powder was calibrated. Then we calibrated the thermoluminescent optical fibre sensor alone and inserted it inside a commercial Li-ion cell (1 Ah). We demonstrate that internal and external temperatures can be monitored during cell cycling at high charge and discharge rates opening the way for the low cost, ease-of-use smart sensing of Li-ion batteries.

2. Materials and Methods

2.1. Characterisation of thermoluminescent particles

$Gd_2O_2S(Er^{3+},Yb^{3+})$ (PTIR545UF) and $NaYF_4(Er^{3+},Yb^{3+})$ (PTIR550F) microparticles were purchased from Phosphor Technology (http://phosphor-technology.com/). The size and morphology of the particles were analysed by Scanning Electron Microscopy (SEM, Hitachi, model S- 5500; 5KV at 15µA). SEM images confirmed the micron size of the commercial particles (*Figure S1* for PTIR545UF and *Figure S2* for PTIR550F, Supporting information). Composition and crystallinity were analysed with a Bruker D8 Advance X-ray powder diffractometer (Cu/Ka radiation source and LynxEye detector). Chemical composition was in good agreement with the supplier's data according to the X-ray diffraction analysis *(Figure S3* for PTIR 545/UF and *Figure S4* for PTIR550F, Supporting information). The luminescence of the powders was measured as received and compared in the same conditions of excitation power and integration time.

2.2. Optical Sensor preparation

To prepare the optical fibre sensor, we used FT200EMT optical fibre from Thorlabs (0.39 NA, Ø200 µm Core Multimode Optical Fibre, low hydroxyl content for 400 - 2200 nm, TECS Clad). The Tefzel® buffer was stripped with mechanical tools and the optical fibre was cloven perpendicularly prior to the coating with particles.

The protocol for particle insertion in silica sol-gel coating at the fibre tip was performed according to the following procedure. To prepare the sol-gel coating, (3-Aminopropyl)triethoxysilane, tetraethoxysilane and poly(methacrylic acid methyl ester), PMMA, average Mw = 350,000, were supplied by Merck Inc. and used without any purification. Optical fibres were cleaned with acetone and placed for 10 minutes in an ultrasound bath in acetone at 303 K before use. Then the optical fibres were dipped in a mixture of 80/20 wt% of tetraethoxysilane/(3-aminopropyl)triethoxysilane under argon atmosphere and stored for 5 minutes at room temperature at 50% relative humidity). The optical fibre with sol coating was put in contact with the phosphor powders, which had previously been finely ground in an agate mortar. The grinding operation served to de-agglomerate the particles to ensure homogeneous insertion in the coating. The modified optical fibres were stored for 1 hour under ammonia vapour to complete the sol-

gel polymerisation at room temperature. Then sample was dried at ambient temperature for 1h. Finally, the modified optical fibres were dipped in a 5 wt% methylene chloride solution of PMMA and dried at room temperature for 1h.

The PMMA is deposited as a protective layer to improve the mechanical properties of the modified optical fibres, we carried out both a coating of high molecular weight PMMA (MW 350,000) in DCM and/or an in situ growth of a highly reticulated PMMA type coating (the outer part of the fibres was previously treated with an isocyanate methacrylate monomer to create a strong urethane bond between the binder and the fibre surface). We did not observe any difference between these two routes in terms of thermal sensing. We therefore concentrated our efforts on the simplest route. We chose PMMA-type materials because we had carried out a screening of polymer stability in new and aged electrolytes by monitoring the swelling of polymer particles (3 mm diameter; molecular weight in the range 35,000 to 450,000) in carbonate electrolytes. By far, the high molecular weight PMMAs showed the best behaviour and were able to survive in the electrolyte for more than 12 months. Some previous studies show the degradation of PMMA by carbonates [44,45]. However, these results concern PMMA with a low molecular weight of around 35,000. In this work we increase the molecular weight up to 350,000 to increase the stability of the PMMA against the carbonate. The stability of the materials used to prepare the sensor has also been demonstrated by the ageing tests presented in this article (see Results section).

Figure S5 (Supporting Information) illustrates the optical microscope (Keyence VHX-500F/VH-Z20R) image of the sensor (optical fibre with thermoluminescent particle coating). We can see in this figure that the coating is located at the end of the fibre with the majority of the particles located on the tip surface. The thickness of the coating is relatively small compared to the diameter of the fibre (less than 10% of the fibre diameter).

2.3. Cell preparation

A non-activated cell (without electrolyte) from Li-FUN Technology Corporation was used for the insertion of the optical fibre sensor. The cell's characteristics are listed in the Table S1. Supporting Information. The active material is $LiNi_{0.6}Mn_{0.2}Co_{0.2}O_2$ (NMC622) as a positive electrode in combination with graphite as a negative electrode. It was a wound pouch cell with a capacity of 1101 mAh measured at a rate of C/20. The instrumentation operations were carried out in the dried room. *Figure S6* (Supporting Information) illustrates the main steps of instrumenting the cell with the thermal sensor. The cell was taken out of the laminated aluminium bag and unrolled over 2 turns. The optical fibre was then placed between the positive electrode and the separator. The foils of the components were then rewound. Additional tabs were welded on the existing tabs and the cell was repackaged in a bag. Two sides of the bag were then sealed with a sealing machine at 453 K. After drying at 328 K under vacuum overnight, the cell was inserted in the glove box and then activated. The electrolyte used was a commercial mixture of ethylene carbonate (EC) and ethyl methyl carbonate (EMC) in a weight ratio of 1:2 with 1M $LiPF_6$ conductive lithium salt and 2 % of vinyl carbonate (VC) additive. Finally, the bag was closed under vacuum. Following the recommendations of the equipment supplier, a degassing step was performed after the formation cycles.

2.4. Optical setup

The luminescent material used for the thermal probe required a light source to excite the Yb^{3+} cations at 980 nm and a spectrophotometer to measure the luminescence peaks of *H*, *S* and *F* transitions in the visible range (between 500 nm and 750 nm). We used an optical fibre coupled withM970F3 LED (970 nm, 5.9 mW, Thorlabs) as the excitation source. The excitation light was transferred through a RP20 (Thorlabs) multimode optical fibre to the sample. It collected the light from the sample and sent it to spectrophotometer. The spectrometer was a compact CCD spectrometer (CCS200, Thorlabs). Multimode optical fibre with a core diameter of 200 µm was used to transport the light between the collimator coupling box and the sample (FT200EMT optical fibre from Thorlabs). An achromatic collimator for multimode fibres (F950SMA-A Thorlabs) was used to measure the powder luminescence in the collimator coupling box. *Figure S7* (Supporting Information) shows a schematic view of the optical test bench for dual luminescence and electrochemistry measurements.

2.5. Sensor calibration

Two different configurations were selected for calibration, depending on the step of the sensor's development and its integration inside the cell (see *Figure S6*, Supporting Information). For the powder calibration, thermoluminescent particles were inserted in a quartz tube and placed in a programmable climatic chamber (Weiss). A thermocouple was fixed inside the tube to measure the temperature of the powder and another one in the centre of the climatic chamber. The luminescence was measured through the quartz by using a collimating lens at the end of the optical fibre. The rest of the optical bench was the same as for the other experiment (optical source, optical fibre, optical element and spectrometer). The climatic chamber was programmed at different temperatures, from 260 to 320 K every 5 K. Each temperature was kept constant for 50 min for thermal stabilisation. During the calibration, the luminescence from the sensor and the temperature from the thermocouple were acquired every 10 s. Luminescence was recorded in a full spectrum range between 200 to 1000 nm.

We proceeded with the same methodology for the optical fibre sensor calibration (alone and inside the cell) except for the optical connection. The optical fibre sensor was directly connected to the test bench *via* the collimator coupling box (see *Figure S7*, Supporting Information). The optical fibre used for the powder calibration was the same type as RP20 fibre (FT-200EMT). The only difference was the collimating lenses between the end of the fibre and the powder sample. This optical component had no significant impact on the luminescent signal.

2.6. Data processing

Post-processing python 3 script was developed for the data post processing. Pandas (v2.4.2), Numpy (1.16.4), Scipy (1.2.1), and Pywavelets (1.0.3) libraries are used for data denoising, analysis and Matplotlib (3.1.0) for data visualisation. The optical signal from the spectrometer was noisy due to the CCD characteristics [46,47] and required the use of denoising techniques. For the data treatment two methods were tested, the first based on the Savitzky-Golay filter (savgol_filter algorithm from Scipy [48]). The second one used the continuous wavelet transform method [49] with the "*coiflets 5"* function [50,51]. *Figure S8* (Supporting Information) shows the results of the noise reduction by these two methods. The grey curve

represents the luminescence intensity ratio between the H and S transitions. The orange curve gives the result after Savitzky-Golay filtering and the red one the result after wavelet filtering. The second method proved to be more powerful and was applied to all the luminescence data.

2.7. Electrochemical cycling.

The pouch cell was placed on a holder and connected to a cycling battery test bench (Bio-logic, VMP3 series). Its effective capacity after formation was 1.017 Ah (C/10, 298 K). To monitor the external temperature, a thermocouple was fixed on the centre of the cell before applying mechanical compression. Constant mechanical stress was applied by a rigid polymer plate and clamps. Two polymer foams were placed between the cell and polymer plate to homogenise the mechanical stress. The cell was tested in the laboratory at constant ambient temperature (298 K). The ambient and surface cell temperatures were measured by thermocouples connected to a data acquisition system (Keysight 34972A + 34910A). The current and cell voltage were measured with the Biologic VMP3 electrochemical bench.

Figure S9 (Supporting Information) shows the current and potential of the cell during cycling. The experiment started with a full charge (State of Charge SOC=100%).

The sequence consisted of:

1- An initial discharge at a constant current of C/5 up to 2.8 V, and a relaxation at I = 0 A for 30 min.
2- A cycle consisting to :
   - a charge at a constant current of C/5 up to 4.2 V that is followed by a second step at constant voltage (4.2V) up to $I \leq C/20$ or 1h (SOC reached = 100%)
   - a discharge at C/5 down to 2.8 V (SOC reached = 0%).
3- A cycle consisting to :
   - a charge at a constant current of C/2 up to 4.2 V that is followed by a second step at constant voltage (4.2V) up to $I \leq C/20$ or 1h (SOC reached = 100%)
   - a discharge at a constant current of 4C down to 2.8 V that is followed by another discharge step at a lower current rate of C/2 down to 2.8 V (SOC reached = 0%). This second step allows the cell to be completely discharged before starting the next charge.
4- A cycle consisting to :
   - a charge at a constant current of 1C up to 4.2 V that is followed by a second step at constant voltage (4.2V) up to $I \leq C/20$ or 1h (SOC reached = 100%)
   - a discharge at a constant current of 4C down to 2.8 V that is followed by another discharge step at a lower current rate of C/2 down to 2.8 V (SOC reached = 0%). This last sequence was repeated 3 times. Discharge at 4C and charge at 2C are the maximum rates for this type of cell. It is well known that cell heating increases with discharge current rate,

especially. Therefore, in order to maximize the temperature increase, we used the maximum discharge rate.

For the ageing test, the cell was submitted to calendar ageing and cycling ageing with protocol of:

1- Calendar ageing:

After the cycling test, the cell was stored for 18 months at SOC 30% in a fridge at T=5°C. The luminescence of the sensor was tested before and after calendar ageing.

2- Cycling ageing:

For the ageing test, the cell was tested in the laboratory at constant ambient temperature (298 K) with the same experimental setup and configuration as in the previous test. The cell was tested with a 2C charge and 4C discharge cycle with the following protocol:

2-1 A low current cycle to evaluate the SOH of the cell, consisting of :
- a charge at a constant current of C/10 up to 4.2 V that is followed by a second step at constant voltage (4.2V) up to $I \leq C/20$ or 1h (SOC reached = 100%)
- a discharge at C/10 down to 2.8 V (SOC reached = 0%).

2-2 150 successive cycles composed of :
- a charge at a constant current of 2C up to 4.2 V that is followed by a second step at constant voltage (4.2V) up to $I \leq C/20$ or 1h (SOC reached = 100%)
- a discharge at 4C down to 2.8 V

Between each charge/discharge, there is a rest period of 30 min.

2-3 A final cycle in the same conditions as sequence 1

3. Results and discussion

Gd_2O_2S (Er^{3+}, Yb^{3+}) (PTIR545UF) was selected as luminescent material for the temperature measurement. This micron sized particle material is an upconverter with a high quantum yield (4.2%) close to the micron-sized $NaYF_4$ (Er^{3+}, Yb^{3+}) (7.8%) [52,53]. The thermoluminescence of this material was studied previously by D. Avram *et al* [51] under excitation at 980 nm and 1550 nm with high pulsed power and continuous laser sources. This material exhibits a higher luminescence under 980 nm excitation with high thermal sensitivity. *Figure 1* compares the luminescence spectra for PTIR545UF (Gd_2O_2S (Er^{3+}, Yb^{3+})) and PTIR550F ($NaYF_4$ (Er^{3+}, Yb^{3+})) at 298K excited at 980 nm (5.9 mW LED). It can be seen that the luminescence of PTIR545UF is seven times higher than PTIR550F. This difference is not due to the quantum yield (QY) but the higher absorption coefficient of Gd_2O_2S(Er^{3+}, Yb^{3+}) compared to $NaYF_4$ (Er^{3+}, Yb^{3+}). QY is not the only parameter for luminescence intensity, the absorption efficiency also play a role. The best comparison between two materials is to compare the luminescence in the same environmental condition with same optical system. In our case we observe that the PTIR545/UF (Gd2O2S:Er^{3+},Yb^{3+}) is more luminescent than (PTIR550/F, NaYF4:Er^{3+},Yb^{3+}), see ***Figure 1***. In our experiment, the luminescence of PTIR545/UF is 7 times more intense than the PTIR550/F. The article by T. Soukka et al [54] shows similar results with the intensity of the peak at 550 nm is 4.71 times more intense for the PTIR545/UF compared to the PTIR550/F.

Due to its higher luminescence intensity, we decided to select PTIR545UF microparticles for the preparation of a thermoluminescent optical fibre sensor.

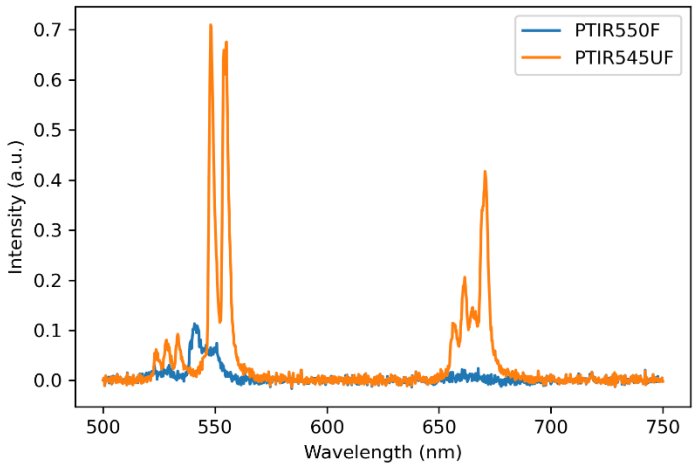

Figure 1. Comparison of luminescence spectra of Gd_2O_2S (Er^{3+}, Yb^{3+}) PTIR545UF and $NaYF_4$ (Er^{3+}, Yb^{3+}) PTIR550F, under 980 nm LED excitation at 298K with the same excitation power and integration time.

Figure 2 shows the upconversion of Gd_2O_2S (Er^{3+}, Yb^{3+}) (PTIR545UF) under excitation at 980 nm and the associated emission spectra in the visible wavelength range (between 500 to 750 nm). Electrons from $^4I_{15/2}$ level of Er^{3+} and Yb^{3+} are excited to a higher energy level by multiple absorptions of infrared photons at 980 nm (bold black arrow). Then electrons return to the lower energy levels by non-radiative transition (dashed arrows) or radiative transition (colored arrows).

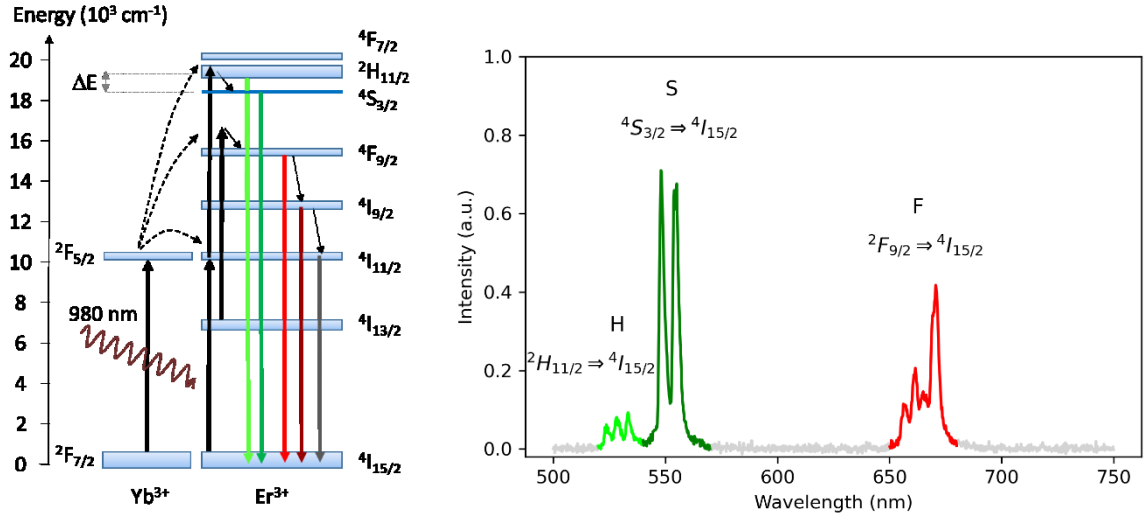

Figure 2. Up-conversion of Gd_2O_2S (Er^{3+}, Yb^{3+}) PTIR545UF under excitation at 980 nm, (left) Energy diagram of Yb^{3+} and Er^{3+} with schematic representation of absorption and radiative transition, (right) up-conversion spectra between 500 to 700 nm at 298 K.

The transitions between excited states ($^2H_{11/2}$, $^4S_{3/2}$ and $^2F_{9/2}$) to the ground state ($^4I_{15/2}$) produce two green and one red emission (labelled H, S and F respectively). The luminescence intensity of these three transitions (H, S and F) depends on the temperature which is why we can use this material as a thermometer. The common approach is to use ratiometry between two peaks of intensity I_1 and I_2, named *FIR* (Fluorescence Intensity Ratio), where the intensity (I) of transition is equal to the area under the peak in luminescence spectra. If we assume the validity of the Boltzmann distribution [32], the intensity ratio between two peaks can be expressed as:

$$FIR = \frac{I_1}{I_2} = Be^{\left(-\frac{\Delta E}{k_B T}\right)} \quad (1)$$

where k_B is the Boltzmann constant, T the temperature, ΔE the energy difference between the barycentre of the two coupled electronic levels ($^2H_{11/2}$, $^4S_{3/2}$), and B is a constant. For the Gd_2O_2S (Er^{3+}, Yb^{3+}), transitions H and S are separated by a small energy gap ΔE ~800 cm^{-1} [52,53] and are used for the temperature measurement by radiometry. In this case I_1 corresponds to the intensity of the H transition and I_2 the intensity of the S transition. From equation (1), $ln(FIR)$ presents a linear variation as a function of $\frac{1}{T}$.

$$\ln(FIR) = \ln\left(\frac{H}{S}\right) = -\frac{\Delta E}{k_B}\left(\frac{1}{T}\right) + \ln(B) \quad (2)$$

Temperature can be estimated by the following equation:

$$T = \frac{\Delta E}{k_B}\frac{1}{\ln(B/FIR)} = \frac{\Delta E}{k_B}\left[\frac{1}{\ln(B)-\ln(FIR)}\right] \quad (3)$$

The uncertainty on temperature can be estimated by [32]:

$$\delta T = \frac{1}{S_r}\frac{\delta FIR}{FIR} \quad (4)$$

Absolute (S_a) and relative (S_r) sensitivities are defined by the following expression. These two parameters were introduced by Collins *et al.* [55] and have been used extensively for comparisons between thermometer performances.

$$S_a = \frac{\partial FIR}{\partial T} \quad (5)$$

$$S_r = \frac{1}{FIR}\left|\frac{\partial FIR}{\partial T}\right| \quad (6)$$

Using $\frac{\partial e^{u(x)}}{\partial x} = \frac{\partial u(x)}{\partial x} e^{u(x)}$, we simplify the expression of absolute sensitivity S_a by:

$$S_a = \frac{\Delta E}{k_B T^2}\, FIR \quad (7)$$

and the expression of the relative sensibility S_r becomes:

$$S_r = \left|\frac{\Delta E}{k_B T^2}\right| \quad (8)$$

S_a depends on the measurement apparatus. S_r is more appropriate for comparing the performances of different thermoluminophores.

The luminescence of PTIR545UF powder has been measured between 283 to 313K; this temperature range is compatible with the expected internal temperature of the 1A.h cell during a cycling test at 298 K. *Figure 3*a shows the variation of luminescence spectra of Gd_2O_2S (Er^{3+}, Yb^{3+}) PTIR545UF as a function of temperature. Each spectrum was normalized on the maximum intensity of the peak corresponding to the *H* transition. A decrease of the peak corresponding to the *S* transition is observed when the temperature increases. The variation of $ln(FIR)$ as a function of $1/T$ (blue point) and the linear regression (redline) are shown on *Figure 3*b. The linear regression coefficient is close to 1.10^3 (K^{-1}) and corresponds to a $\Delta E = 695\ cm^{-1}$. This value is very close to the value of ~ 700 cm^{-1} found by D. Avram et al. [52] and also close to the theoretical energy gap between the H and S transition $\Delta E = 800\ cm^{-1}$. The relative sensitivity (S_r) is between 1.25 and 1.00 %. K^{-1} in the range of temperature between 280 to 315 K, which is in agreement with the values reported in the literature [29,31].

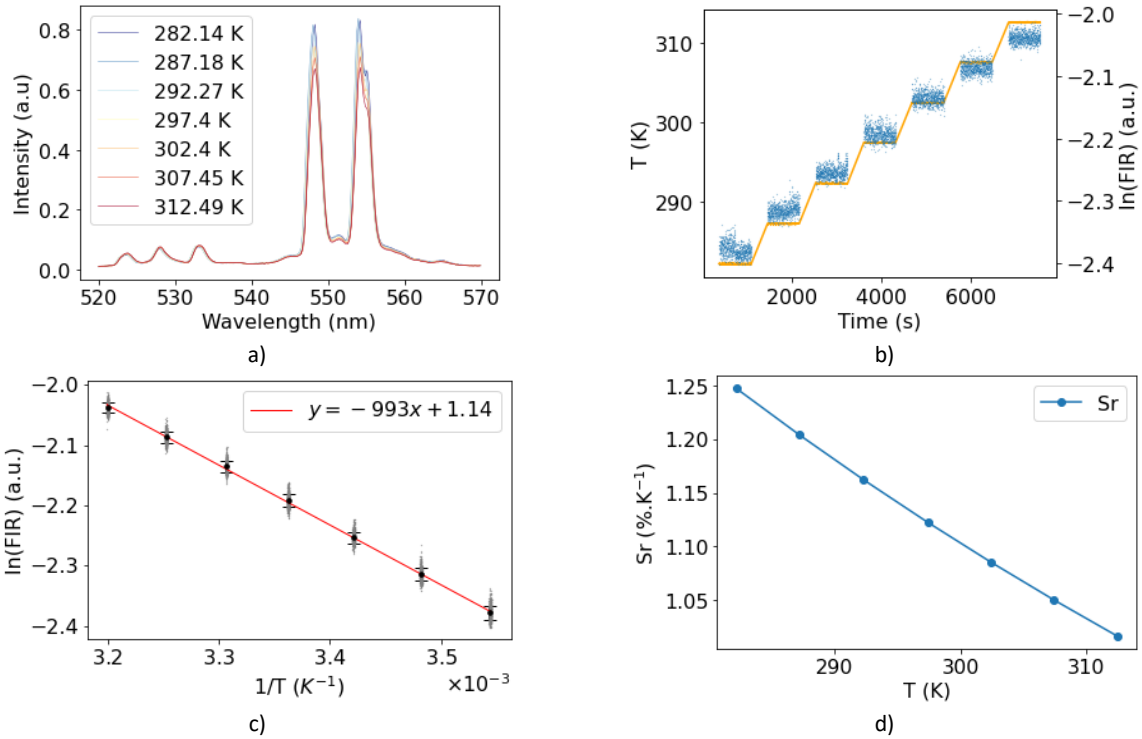

Figure 3. Thermoluminescence of Gd2O2S (Er3+, Yb3+) PTIR545UF powder: a) Evolution of luminescence spectra between 282 to 312 K, (b) Ln(*FIR*) (blue point) and Temperature (orange line) variation as a function of time during calibration, (c) Linear variation of ln(*FIR*)=f(1/T): measure (grey), mean and error bar correspond to the root mean square RMS (dark) and linear regression (red). (d) Relative sensitivity (S_r) as a function of temperature calculated from linear regression coefficients (ln(*FIR*)=f(1/T)).

The temperature dependence of luminescence was tested with the same protocol for both the optical fibre sensor and for optical fibre sensors embedded inside of the cell. The results obtained for the optical fibre sensor are shown in *Figure 4*. The variation of *ln(FIR)* as a function of *1/T* has a slope of 1044 (K^{-1}), which is close to the slope calculated for the Gd_2O_2S (Er^{3+}, Yb^{3+}) PTIR545UF powder. This comparison indicates that the insertion of the luminescent particles into the silica matrix covered by a PMMA layer (as a protective layer) at the end of optical fibre does not affect the performances of the thermoluminescent particles. A small intensity difference is observed in the two luminescence peaks of the *S* transition between the powder and the optical fibre sensor. The intensity of the second peak of the *S* transition is smaller than the first one for optical fibre sensor (*Figure 4a*). This variation is due to the absorption of the optical fibre itself and does not affect the performances of the thermal probe (*Figure 4*). Furthermore, the same linear variation of ln(*FIR*) as function of 1/T in *Figures 3a* and *4a* confirms that the introduction of thermoluminescent particles in the sol matrix surrounded with a protective layer does not affect their thermoluminescence properties. The relative sensitivity (S_r) of the optical fibre is slightly higher than that of the thermoluminescent particles, with a range of 1.10 to 1.45 $\%.K^{-1}$ for temperature in the same temperature range (from 312 to 272 K).

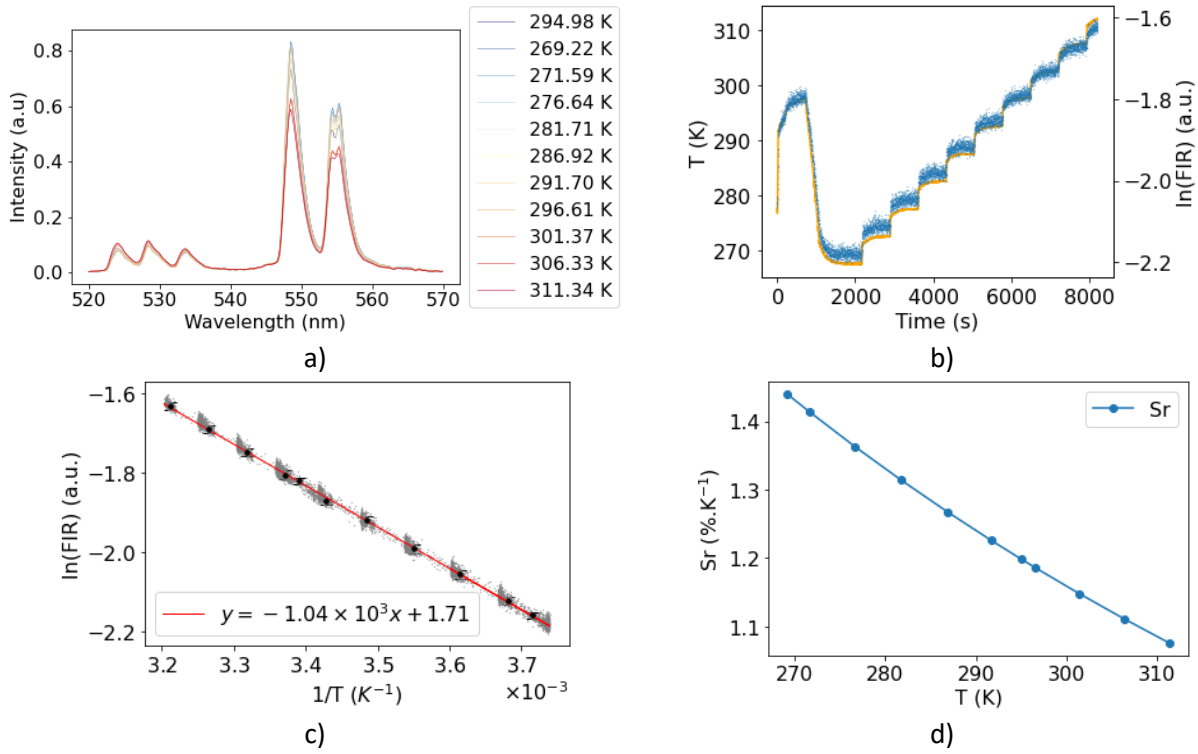

394 **Figure 4**. Thermoluminescence of optical fibre with Gd2O2S (Er3+, Yb3+) PTIR545UF powder (in the silica matrix) and PMMA
395 coating: a) Luminescence spectra evolution between 272 to 312 K, (b) Ln(*FIR*) (blue point) and Temperature (orange line) variation
396 as a function of time during calibration, (c) Linear variation of ln(*FIR*)=f(1/*T*): measure (grey), mean and error bar error bar
397 correspond to the root mean square RMS (dark) and linear regression (red) . (d) Relative sensitivity (S_r) as a function of
398 temperature calculated from the linear regression coefficients (ln(*FIR*)=f(1/*T*)).

399

400 The same results were obtained for the calibration of the optical fibre inserted inside the Li-ion cell (*Figure*
401 *5*). There is no observable modification of the emission spectrum due to the insertion of the sensor inside
402 the cell. The slope of the ln(*FIR*) as a function of (1/*T)* is equal to the slope before the insertion (1044 (K^{-1})). The S_r value is very similar to the value obtained with the optical fibre before insertion inside the cell.
404 A small variation of the shape of the second peak of the *S* transition is observed due to the difference of
405 the length of the optical fibre between the thermal probe and the spectrophotometer. However, the slope
406 of the linear regression in ln(*FIR*) as a function of (1/*T*) is close to the previous value, around 1000 (K^{-1}).
407 The relative sensitivity S_r varied between 1.1 and 1.4 between 308 and 270 K. All these measurements
408 show several small variations in the calibration of sensors depending on the environment and the
409 measurement system. Although the variations are small, it is necessary to calibrate the sensor inside the
410 cell to obtain optimum accuracy. When calibrating of the sensor inside the cell we decide to add a
411 temperature step at 300K at the beginning of the calibration protocol (see ***Figure 5***). The aim is to evaluate
412 if the sensor is sensitive to the order of the temperature during calibration. In the results (***Figure 5***) all the
413 points are well aligned and we conclude that there is no memory effect when there is a sudden
414 temperature change related to the cooling or heating.

415

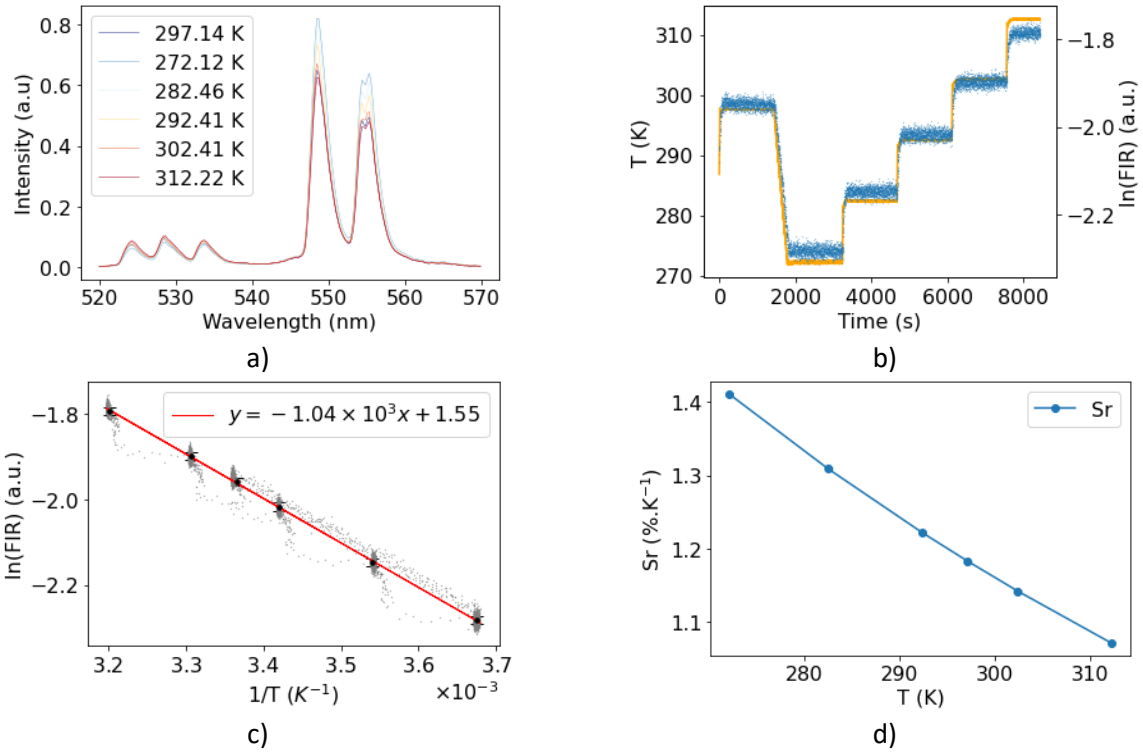

Figure 5. Thermoluminescence of optical fibre with Gd2O2S (Er3+, Yb3+) PTIR545UF powder in silica matrix and PMMA coating inside the Li-ion cell: a) Luminescence spectra evolution between 272 to 312 K, (b) Ln(*FIR*) (blue point) and Temperature (orange line) variation as a function of time during calibration, (c) Linear variation of ln(*FIR*)=f(1/T): measure (grey), mean and error bar correspond to the root mean square RMS (dark) and linear regression (red). (d) Relative sensitivity (S_r) as a function of temperature calculated from the linear regression coefficient (ln(*FIR*)=f(1/*T*)).

The accuracy of the optical probe (powder) and the sensor was calculated from the calibration data. The variance (δFIR) of the FIR from the theoretical value (FIR_{th}) for each temperature was calculate from the equation (9) below:

$$\delta FIR = \frac{FIR}{FIR_{th}} \quad (9)$$

Where FIR_{th} is calculated from equation (2) with the linear coefficients $-\frac{\Delta E}{k_B}$ and B determined by calibration data (***Figure 4*** for optical probe and ***Figure 5*** for sensor). The temperature measurement error δT is calculated from the equation (4). The Figure S10 and S11 show the δFIR and δT as a function of T for the sensor alone and inserted in the cell. The uncertainty of the temperature δT is about +/- 1°C over the range tested. A higher value for the error between two constant temperature plateaus is shown in Figure S11 for the sensor inside the cell. This error is not related to the sensor but to the thermal gradient between the sensor temperature inside the cell and the reference temperature measured in the climate chamber during the temperature transition. These points are outliers. They are not taken into account when evaluating the accuracy of the sensor.

Figure 6 shows the variation of the maximum luminescence for the peak at 548 nm (S transition) over time with the cell potential *U*(V), cell current *I*(A) and cell surface temperature T_{ext} (K). The correlation between the external temperature and the *S* transition peak variation is shown clearly. The S peak intensity decreases when the temperature increases during the cell charge at a rate of 1C and discharge at a rate of

4C. The variation of luminescence during discharge at a rate of 4C is greater than the charge at a rate of 1C due to a higher rise in temperature.

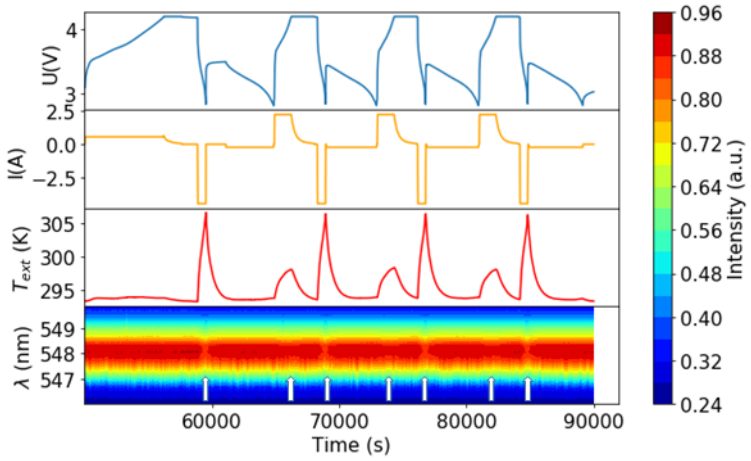

Figure 6. Variation of the cell potential *U*(V), cell current *I*(A), external cell temperature T_{ext} and luminescence variation of the S transition (maximum peak at 548 nm). The arrow highlights the signal variation in the spectrum when the temperature increases.

Figure 7 represents the measurement of cell potential (*U*), cell current (*I*), external temperature (T_{ext}) from a thermocouple sensor and internal temperature (T_{int}) from our luminescent sensor. During the first charge and discharge steps at low C-rates, the temperature of the cell does not change. The surface temperature increases during the discharge at 4C up to 14 K and charge at 1C up to 5 K in comparison with the ambient temperature (see *Figure 8*).

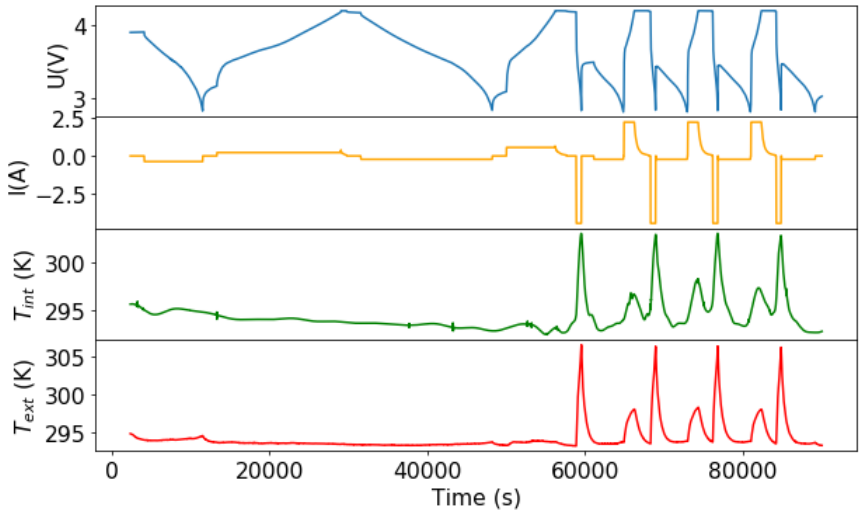

Figure 7. Internal and external cell temperature variations during cell cycling

The temperature variation is clearly correlated with the charge and discharge profiles. The shape and the intensity of the temperature variations are similar to those in the literature for this type of Li-ion cell [56]. The signal from the thermoluminescent sensor shows the same variation over time with good correlation with the surface temperature measurement. The cell used for this experiment was a pouch cell with a small capacity (1A.h). The Biot number (B_i) can be calculated to evaluate if there is a difference between the internal and external temperatures. The Biot number is defined as:

$$B_i = \frac{hL_c}{\lambda_b} \quad (10)$$

where h is the global thermal transfer coefficient (0.5 W/m/K), L_c the characteristic length, in our case half of the cell thickness (1 mm), λ_b the thermal conductivity (0.5W/m/K).

In our case the Biot number is very small (0.04) and much lower than 0.1. Thus, it can be considered that the gradient between the centre and the surface is less than 1K [57,58]. We can conclude that the internal temperature measurement should be close to the external temperature measured at the surface of the cell, which is in agreement with the measurements performed with the optical sensor.

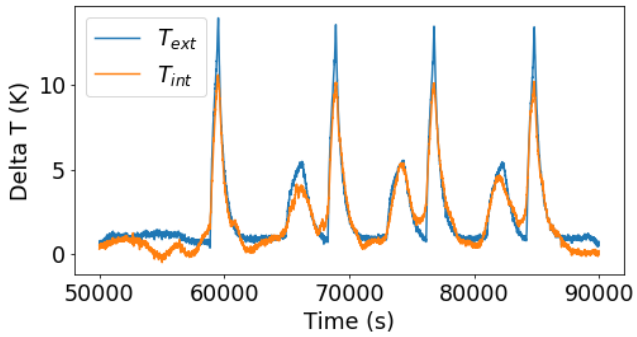

Figure 8. Temperature variation from ambient: comparison between external and internal measurement during cell cycling.

The variation of the signal during the first step at a low C-rate is probably due to the stability of the light source. *Figure 8* displays variations of the baseline for the luminescence sensor and a lower value for the four peaks during 4C discharge. This difference is attributed to the loss of accuracy during signal denoising (*Figure S8*. Supporting Information). To limit this effect and increase the accuracy of the sensor, optical optimisation is required to limit the noise and increase the luminescence signal.

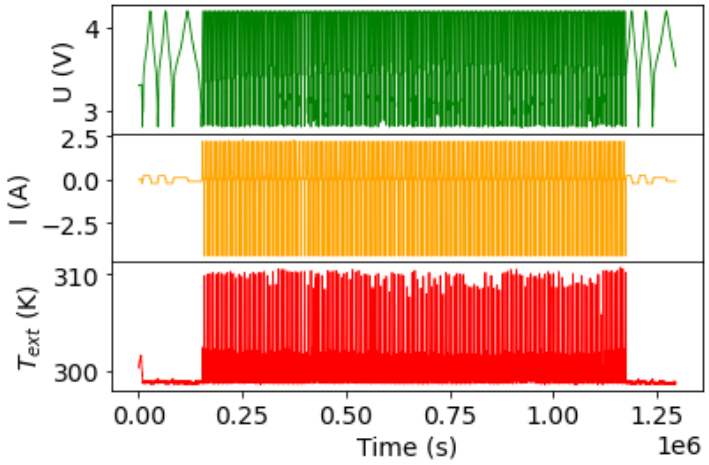

a)

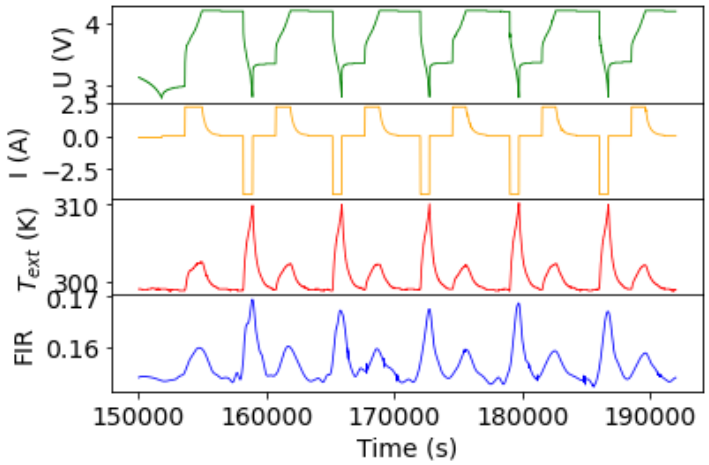

b)

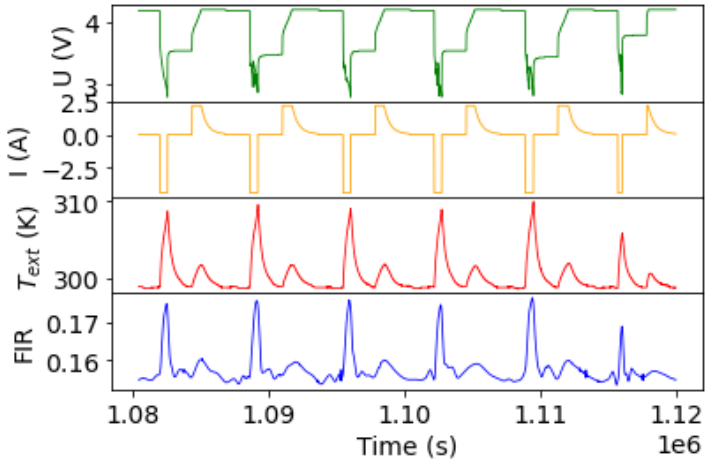

c)

Figure 9: Aging result during cycling test. a) Full view of the cycling test with the variation of the cell potential (U), the cell current (I) and the external temperature of the cell T_{ext} measured by thermocouple. Zoom of the 5 first cycles (b) and the 6 last cycles (c) with the luminescence ratio correlate to the Text, I and U cell.

The results of the ageing test are shown in the Figure 9. The external cell temperature (T_{ext}), current (I) and potential (V) are shown in the Figure 9. a). A zoom of the 5 first and 6 last cycles are shown in the Figure

9. b) and Figure 9. c) represent the chronogram of the variation of the optical signal from the sensor (FIR) compared to the T_{ext} measurement, cell current and cell potential. The variation of the SOH_{2C} and SOH_{4D} variation during ageing is shown in the Figure S13 (Supplementary data). SOH_{2C} is defined as the ratio of the capacity charged at 2C during the cycle n divided by the capacity charged at 2C during the first cycle. SOH_{4D} is calculated in the same way with the discharge capacity during the discharge at 4D. The maximum temperature reached during the charge phase at 2C and the discharge phase at 4D are plotted in figure S14. In both figures we can see the degradation rate of the cell. After 150 cycles, about 15% of the capacity is lost in the charge (2C) and discharge (4D) phases. The maximum temperature of the cell (text) during the 2C charge decreases by less than 0.25°C. The mean value of the maximum temperature during the discharge phase at 4D remains constant during ageing. However, we observe a greater dispersion of the maximum temperature during discharge at 4C. This dispersion is related to the dispersion of the discharge capacity during ageing. This dispersion becomes more important as the number of cycles increases. It's a sign of the degradation of the cell's performance. This degradation is visible in the cell potential during discharge at 4C (see green curve in Figure 9).

For the optical sensor, we can see in Figure 9 b) and c) that the FIR signal is correlated with the cell temperature during all the ageing test. These results demonstrate the good stability of the sensor in the high C-rate condition over 150 cycles. After 150 cycles, we can see that the intensity of the signal from the sensor has not been affected by the ageing of the cells.

4. Conclusions and perspectives

We demonstrated the interest of using thermoluminescent material as a thermal probe to monitor the internal temperature of a lithium ion cell during fast charging. For the first time, $Gd_2O_2S:Er^{3+},Yb^{3+}$ was used as a thermal probe in combination with an optical fibre sensor to monitor internal cell temperature during cycling at high current in charges and discharges with a low cost and compact excitation and detection system. This material has a higher luminescence than $NaYF_4:Er^{3+},Yb^{3+}$ previously described by H. Li et al. [43], and has a high relative sensitivity (1.25 $\%.K^{-1}$ at 280 K). We demonstrated that the thermoluminescence performances of $Gd_2O_2S:Er^{3+},Yb^{3+}$ are not affected by the preparation of the optical fibre sensor, even after the insertion of the sensor inside the Li-ion cell. We showed that insertion inside the cell does not affect the performance of the cell and that measurement is possible at high corresponding C-rates (fast charging and high power loading of the cell). These results validate the interest of this kind of sensor for use in battery management systems. The use of LEDs as optical sources reduces the cost of this type of sensor compared with other optical fibre sensors used previously for temperature monitoring in Li-ion batteries. The instrumented cell with sensor was tested in ageing (calendar during 18 months) and over 150 cycling at high c-rate. The optical signal of the sensor shows no major degradation after the ageing test. These results show the stability of the sensor in the environment and justify the choice of materials. In the future, it will be interesting to carry out tests over a longer period of time and under different conditions in order to characterise the durability of the sensor more fully. Furthermore, the results published on the use of internal cell temperature sensors with fibre optics only concern a few cycles[59]. To the best of our knowledge, the results presented here of 150 cycles at high C-rate in charge and discharge presented here are new.

In terms of accuracy, this sensor is less sensitive than FBG type sensors (1°C versus 0.1°C). However, this accuracy is sufficient to characterise high capacity cells for fast charge and discharge. This accuracy can be improved by increasing the power of the optical source and the sensitivity of the detection system. In addition, other work on thermoluminescence shows that it is possible to use this technique to achieve a resolution comparable to the FBG of 0.1°C [29,32]. However, this comes at an increased cost. The advantage of this solution over an FBG-type sensor is precisely its lower cost. For example, the cost of the spectrophotometer for this sensor is 15 times lower than for an FBG interrogator with a resolution of 0.1°C.

We conclude that this new thermal sensor based on functionalised optical fibre is a good candidate for achieving the goals of the BATTERY2030+ roadmap and for the development of smart batteries [4].

The outlook for this work is to further increase sensor sensitivity by improving the optical component and signal post-treatment to reduce signal noise. The long-term stability of this type of sensor still needs to be studied; likewise for its integration into an industrial cell manufacturing process. These results open the way to a producing a new sensitive thermal sensor for monitoring the internal temperature of Lion cells.

Credit authorship contribution statement

Olivier Raccurt: Conceptualization, Writing - Original draft, Visualization, Project administration & supervision, funding acquisition. Elise Villemin, Sylvie Genies, Cédric Septet and Pierre Balfet: Cell fabrication and instrumentation, Experiment preparation, Electrochemistry tests and Results analysis, Writing, review & editing. Olivier Poncelet & Sonia Desousa-Nobre: Optical fibre sensor preparation and Optical characterisation, Writing, review & editing. Romain Franchi: Development of the platform for data acquisition and visualisation. Jérôme Houny & Martin Guillon: Calibration of the sensor, data treatment, Writing, review & editing.

Declaration of competition interest

The authors declare that they have no known competing financial interests or personal relationships that could have appeared to influence the work reported in this paper. There are no conflicts to declare.

Data availability

The data that support the findings of this study are available from the corresponding author upon reasonable request.

Supplementary materials

Supplementary material associated with this article can be found at the end of these file.

Acknowledgements

The INSTABAT project has received funding from the European Union's Horizon 2020 research and innovation programme under grant agreement No. 955930. INSTABAT carried out in the framework of the BATTERY2030+ large scale initiative under grant agreement No. 957213. The authors would like to thank Didier Buzon (CEA) for fruitful discussion on the assessment of the thermal gradient between the internal and external temperatures of the cell and the explanation of the Biot number. The authors would also like to thank Charlotte Gervillé and Jean-Marie Tarascon (CNRS Collège de France) for providing the LiFun cell

in the framework of the INSTABAT project. Lastly, the authors would like to thank Konstantin Tarasov (CEA) for the X-ray analysis of thermoluminescent particles, Marco Ranieri (CEA) for her contribution to ageing test and Sandrine Lyonnard (CEA) for her comments on the results analysis and the publication content.

References

[1] H. A. Gabbar, A. M. Othman, M. R. Abdussami, *Technologies* **2021**, *9*, 28.
[2] X. Lu, J.-M. Tarascon, J. Huang, *eTransportation* **2022**, *14*, 100207.
[3] Z. Wei, J. Zhao, H. He, G. Ding, H. Cui, L. Liu, *J. Power Sources* **2021**, *489*, 229462.
[4] J. Amici, P. Asinari, E. Ayerbe, P. Barboux, P. Bayle-Guillemaud, R. J. Behm, M. Berecibar, E. Berg, A. Bhowmik, S. Bodoardo, I. E. Castelli, I. Cekic-Laskovic, R. Christensen, S. Clark, R. Diehm, R. Dominko, M. Fichtner, A. A. Franco, A. Grimaud, N. Guillet, M. Hahlin, S. Hartmann, V. Heiries, K. Hermansson, A. Heuer, S. Jana, L. Jabbour, J. Kallo, A. Latz, H. Lorrmann, O. M. Løvvik, S. Lyonnard, M. Meeus, E. Paillard, S. Perraud, T. Placke, C. Punckt, O. Raccurt, J. Ruhland, E. Sheridan, H. Stein, J.-M. Tarascon, V. Trapp, T. Vegge, M. Weil, W. Wenzel, M. Winter, A. Wolf, K. Edström, *Adv. Energy Mater.* **2022**, *12*, 2102785.
[5] 'Battery 2030+ Large Scale Initiative'. [Online]. Available: https://battery2030.eu/, Accessed: Apr. 24, 2023
[6] T. Waldmann, M. Wilka, M. Kasper, M. Fleischhammer, M. Wohlfahrt-Mehrens, *J. Power Sources* **2014**, *262*, 129.
[7] L. H. J. Raijmakers, D. L. Danilov, R.-A. Eichel, P. H. L. Notten, *Appl. Energy* **2019**, *240*, 918.
[8] K. A. Wickersheim, M. H. Sun, *J. Microw. Power Electromagn. Energy* **1987**, *22*, 85.
[9] Q. Wu, M. Mikolajek, R. Martinek, J. Koziorek, S. Hejduk, J. Vitasek, A. Vanderka, R. Poboril, V. Vasinek, R. Hercik, *J. Sens.* **2020**, *2020*, 8831332.
[10] J. Hedman, R. Mogensen, R. Younesi, F. Björefors, *Adv. Mater. Interfaces* **2023**, *10*, 2201665.
[11] J. Hedman, R. Mogensen, R. Younesi, F. Björefors, *ACS Appl. Energy Mater.* **2022**, *5*, 6219.
[12] J. Hedman, F. Björefors, *ACS Appl Energy Mater* **2022**, *5*, 870.
[13] J. Huang, L. Albero Blanquer, J. Bonefacino, E. R. Logan, D. Alves Dalla Corte, C. Delacourt, B. M. Gallant, S. T. Boles, J. R. Dahn, H.-Y. Tam, J.-M. Tarascon, *Nat. Energy* **2020**, *5*, 674.
[14] C. Modrzynski, V. Roscher, F. Rittweger, A. Ghannoum, P. Nieva, K. Riemschneider, in *2019 IEEE Sens.*, **2019**, pp. 1–4.
[15] J. Hedman, D. Nilebo, E. Larsson Langhammer, F. Björefors, *ChemSusChem* **2020**, *13*, 5731.
[16] M. Nascimento, T. Paixão, M. S. Ferreira, J. L. Pinto, *Batteries* **2018**, *4*, 67.
[17] M. Nascimento, M. S. Ferreira, J. L. Pinto, *Appl. Therm. Eng.* **2019**, *149*, 1236.
[18] M. Nascimento, M. S. Ferreira, J. L. Pinto, *Measurement* **2017**, *111*, 260.
[19] A. Ghannoum, K. Iyer, P. Nieva, A. Khajepour, in *2016 IEEE Sens.*, **2016**, pp. 1–3.
[20] A. Ghannoum, R. C. Norris, K. Iyer, L. Zdravkova, A. Yu, P. Nieva, *ACS Appl. Mater. Interfaces* **2016**, *8*, 18763.
[21] A. Ghannoum, P. Nieva, *J. Energy Storage* **2020**, *28*, 101233.

[22] A. Ghannoum, P. Nieva, A. Yu, A. Khajepour, *ACS Appl. Mater. Interfaces* **2017**, *9*, 41284.
[23] M. Nascimento, S. Novais, M. S. Ding, M. S. Ferreira, S. Koch, S. Passerini, J. L. Pinto, *J. Power Sources* **2019**, *410–411*, 1.
[24] A. Fortier, M. Tsao, N. D. Williard, Y. Xing, M. G. Pecht, *Energies* **2017**, *10*, 838.
[25] J. Unterkofler, G. Glanz, M. Koller, R. Klambauer, A. Bergmann, *Batteries* **2023**, *9*, 34.
[26] J. Xi, J. Li, H. Sun, T. Ma, L. Deng, N. Liu, X. Huang, J. Zhang, *Sens. Actuators Phys.* **2022**, *347*, 113888.
[27] J. Bonefacino, S. Ghashghaie, T. Zheng, C.-P. Lin, W. Zheng, L. A. Blanquer, J. Huang, C. Gervillié, H.-Y. Tam, J.-M. Tarascon, S. T. Boles, *J. Electrochem. Soc.* **2022**, *169*, 100508.
[28] L. Matuck, J. L. Pinto, C. Marques, M. Nascimento, *Batteries* **2022**, *8*, 233.
[29] C. D. S. Brites, S. Balabhadra, L. D. Carlos, *Adv. Opt. Mater.* **2019**, *7*, 1801239.
[30] M. D. Dramićanin, *Methods Appl. Fluoresc.* **2016**, *4*, 042001.
[31] X. Wang, O. S. Wolfbeis, R. J. Meier, *Chem Soc Rev* **2013**, *42*, 7834.
[32] C. D. S. Brites, A. Millán, L. D. Carlos, in *Handb. Phys. Chem. Rare Earths* (Eds.: J.-C. G. Bünzli, V. K. Pecharsky), Elsevier, **2016**, pp. 339–427.
[33] B. Li, F. Zhang, W. Liu, X. Chen, Y. Gao, Q. Zhang, X. Yan, F. Wang, X. Zhang, T. Suzuki, Y. Ohishi, T. Cheng, *IEEE Trans. Instrum. Meas.* **2022**, *71*, 1.
[34] S. Sánchez-Escobar, J. Hernández-Cordero, *Opt Lett* **2019**, *44*, 1194.
[35] K. T. V. Grattan, Z. Y. Zhang, in *Opt. Fiber Sens. Technol. Chem. Environ. Sens.* (Eds.: K. T. V. Grattan, B. T. Meggitt), Springer Netherlands, Dordrecht, **1999**, pp. 133–203.
[36] M. K. Shahzad, Y. Zhang, M. U. Khan, X. Sun, L. Liu, H. Li, *Opt Mater Express* **2018**, *8*, 2321.
[37] H. E. Benjamin R. Anderson Steven Livers, Ray Gunawidjaja, *Opt. Eng.* **2019**, *58*, 097105.
[38] J. Thiem, S. Spelthann, L. Neumann, F. Jakobs, H.-H. Johannes, W. Kowalsky, D. Kracht, J. Neumann, A. Ruehl, D. Ristau, *Sensors* **2020**, *20*, 6048.
[39] J. J. Talghader, M. L. Mah, E. G. Yukihara, A. C. Coleman, *Microsyst. Nanoeng.* **2016**, *2*, 16037.
[40] M. D. Dramićanin, *J. Appl. Phys.* **2020**, *128*, 040902.
[41] A. Nexha, J. J. Carvajal, M. C. Pujol, F. Díaz, M. Aguiló, *Nanoscale* **2021**, *13*, 7913.
[42] X. Han, L. Lu, Y. Zheng, X. Feng, Z. Li, J. Li, M. Ouyang, *eTransportation* **2019**, *1*, 100005.
[43] H. Li, F. Wei, Y. Li, M. Yu, Y. Zhang, L. Liu, Z. Liu, *J Mater Chem C* **2021**, *9*, 14757.
[44] C. Rizzuto, D. C. Teeters, R. C. Barberi, M. Castriota, *Gels* **2022**, *8*, DOI 10.3390/gels8060363.
[45] E. R. Nimma, S. Kalyanasundaram, Y. Saito, A. M. Stephan, *Polimeros* **2005**, *15*, 46, DOI 10.1590/S0104-14282005000100011.
[46] C. Huang, G. Xia, S. Jin, M. Hu, S. Wu, J. Xing, *Optik* **2018**, *157*, 693.
[47] K. Naveed, S. Ehsan, K. D. McDonald-Maier, N. Ur Rehman, *Sensors* **2019**, *19*, 206.
[48] 'Scipy'. Accessed: Apr. 24, 2023. [Online]. Available: https://docs.scipy.org/doc/scipy/reference/generated/scipy.signal.savgol_filter.html
[49] Ataspinar, "A guide-for using the wavelet transform in machine learning," **2018**.
[50] 'Pywavelets'. Accessed: Apr. 24, 2023. [Online]. Available: https://pywavelets.readthedocs.io/en/latest/
[51] 'wavelet coif5'. Accessed: Apr. 24, 2023. [Online]. Available: https://wavelets.pybytes.com/wavelet/coif5/
[52] D. Avram, C. Tiseanu, *Methods Appl. Fluoresc.* **2018**, *6*, 025004.

[53] M. Pokhrel, G. A. Kumar, D. K. Sardar, *J Mater Chem A* **2013**, *1*, 11595.
[54] T. Soukka, K. Kuningas, T. Rantanen, V. Haaslahti, T. Lövgren, *J. Fluoresc.* **2005**, *15*, 513.
[55] S. F. Collins, G. W. Baxter, S. A. Wade, T. Sun, K. T. V. Grattan, Z. Y. Zhang, A. W. Palmer, *J. Appl. Phys.* **1998**, *84*, 4649.
[56] S. Goutam, J.-M. Timmermans, N. Omar, P. V. den Bossche, J. Van Mierlo, *Energies* **2015**, *8*, 8175.
[57] P. Taheri, M. Yazdanpour, M. Bahrami, *J. Power Sources* **2013**, *243*, 280.
[58] S. A. Hallaj, H. Maleki, J. S. Hong, J. R. Selman, *J. Power Sources* **1999**, *83*, 1.
[59] Z. Xiao, C. Liu, T. Zhao, Y. Kuang, B. Yin, R. Yuan, L. Song, *J. Electrochem. Soc.* **2023**, *170*, 057517.

Supplementary Information

Thermo-luminescent optical fibre sensor for Li-ion cell internal temperature monitoring

Elise Villemin[1], Sylvie Genies[1], Olivier Poncelet[2], Pierre Balfet[1], Cédric Septet[1], Romain Franchi[1], Martin Guillon[1], Jérôme Houny[1], Sonia Sousa-Nobre[2], Olivier Raccurt[1*]

[1] Univ. Grenoble Alpes, CEA, LITEN, DEHT, F-38000 Grenoble, France

[2] Univ. Grenoble Alpes, CEA, LITEN, DTNM, F-38000 Grenoble, France

* Corresponding author: olivier.raccurt@cea.fr

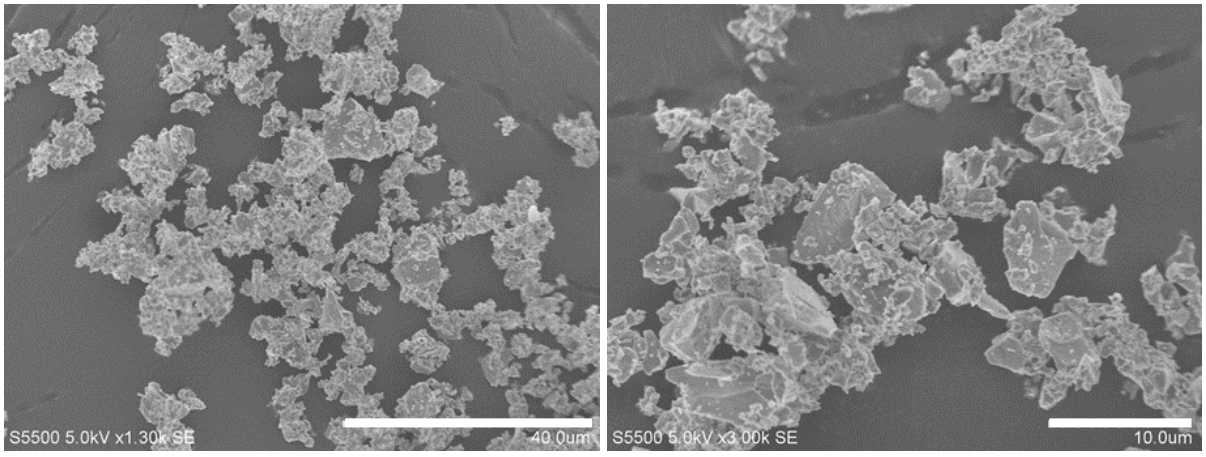

Figure S10: Scanning Electronic Microscope image of PTIR545UF $Gd_2O_2S:Er^{3+},Yb^{3+}$ Powder. Left: scaling x1300, scaling bare: 40 µm. Right: scaling x3000, scaling bare: 10 µm.

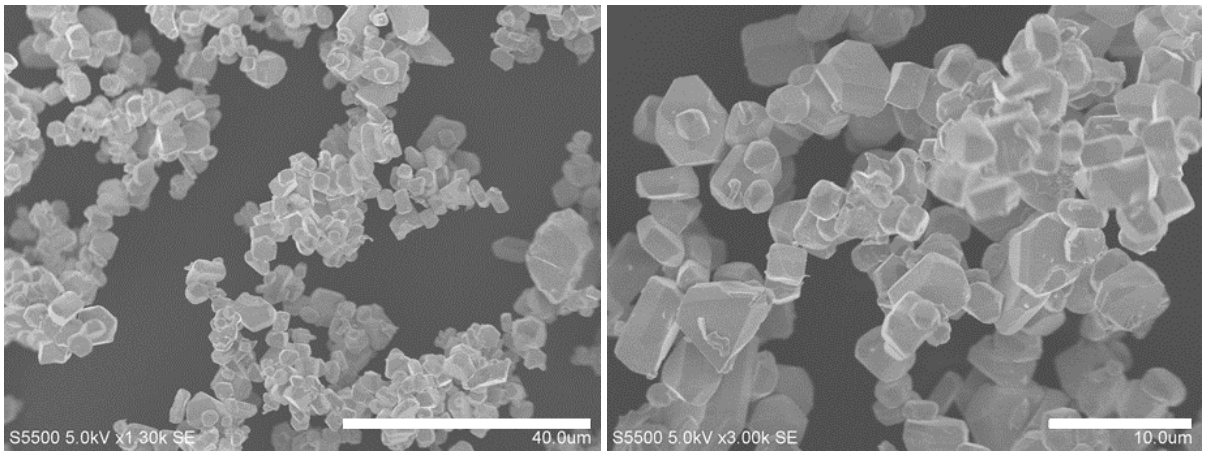

Figure S11: Scanning Electronic Microscope image of PTIR550F $NaYF_4:Er^{3+},Yb^{3+}$ powder. Left: scaling x1300, scaling bare: 40 µm. Right: scaling x3000, scaling bare: 10 µm.

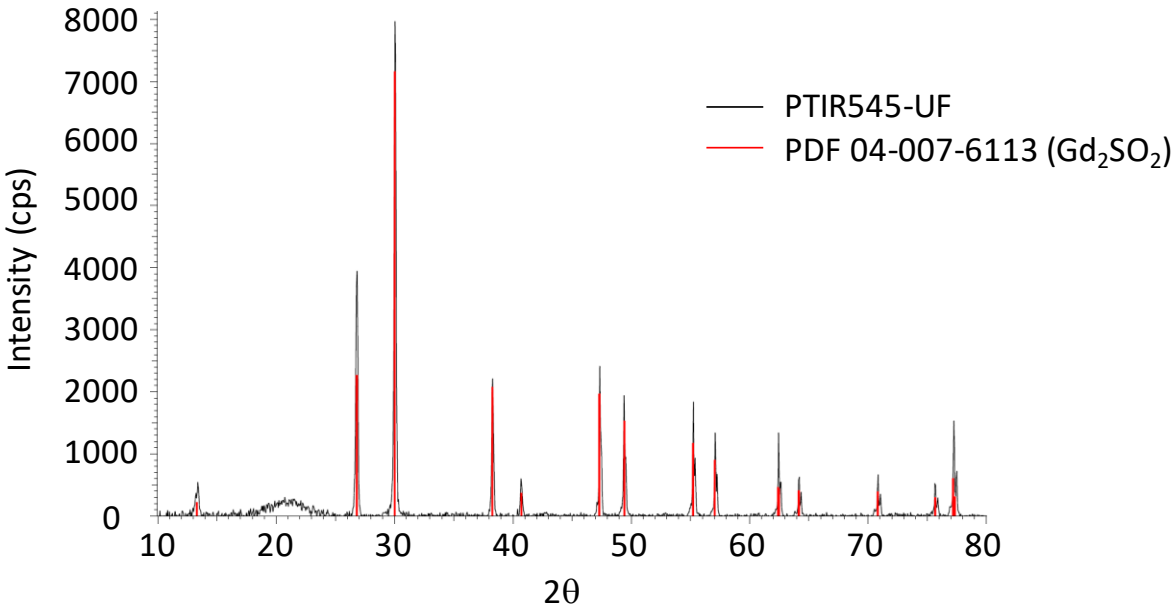

Figure S12: X-ray diffraction analysis (XRD) of PTIR545-UF powder compared to the reference PDF 04-007-6113 (ICCD) for Gd_2SO_2 material.

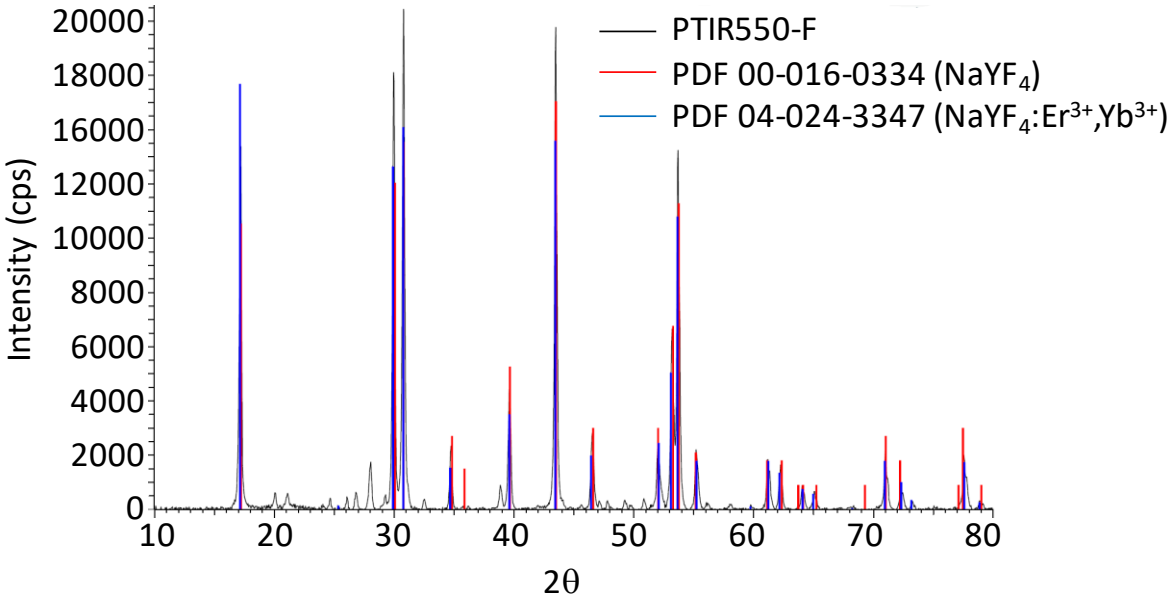

Figure S13: X-ray diffraction analysis (XRD) of PTIR550-F powder compared to the reference PDF 00-016-0334 (ICCD) for $NaYF_4$ material and the reference PDF 04-024-3347 (ICCD) for $NaYF_4$:Er^{3+},Yb^{3+} material.

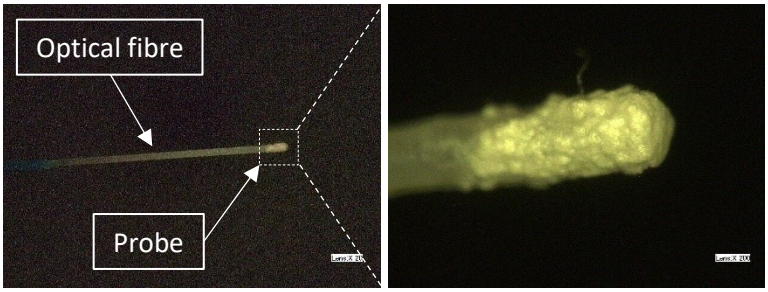

Figure S14: Optical microscope image of the sensor. (Left): Optical fibre with the thermoluminescent particles on the tip (x20), (right) close-up of the end of the tip (x200).

Table S1: Cell characteristics.

Electrochemical characteristics	
Voltage range (V)	3.0 - 4.2
Average voltage (V)	3.7 at room temperature and 0.2 C
Optimal capacity (mAh)	1100 mAh at room temperature and 0.2 C
Positive real capacity (mAh/cm²)	1100 mAh at room temperature and 0.2 C
Positive real capacity (mAh/cm²)	2.8
Energy density (Wh/kg)	214
Energy density (Wh/L)	425
Cathode	
Material	NMC622
Active material loading (%)	96.4
press density (g/cc)	3.30
Coating Weight (mg/cm²)	16.7
Anode	
Material	Graphite
Active material loading (%)	94.8
press density (g/cc)	1.8
Coating Weight (mg/cm²)	10
Separator	
Material	PE with Al_2O_3 coating on NMC side
Thickness	15 µm

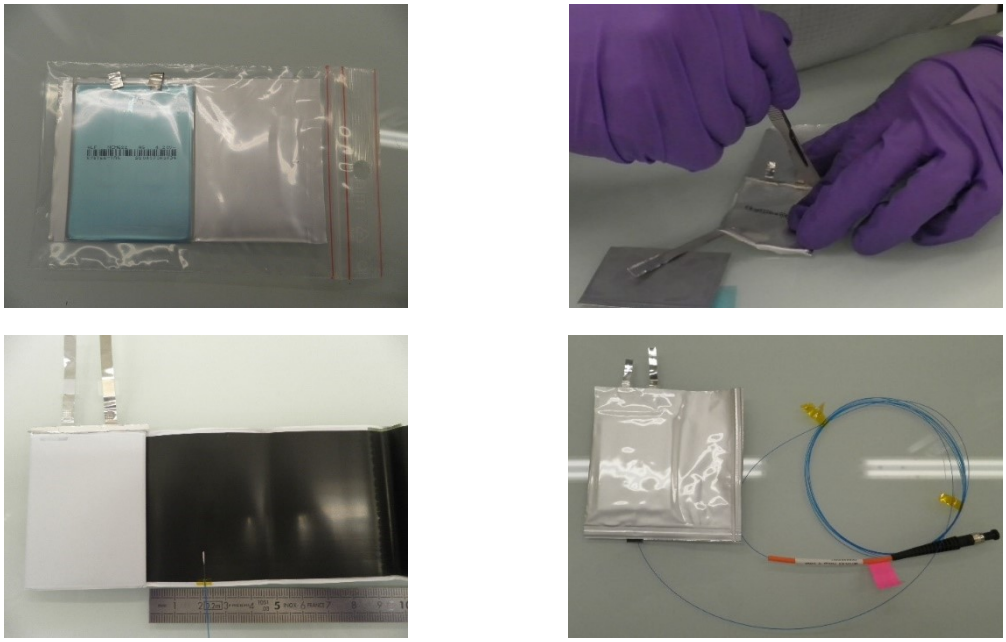

Figure S15: Cell instrumentation: Non-activated commercial cell (top, left), Cell opening (top, right), optical fibre sensor insertion (bottom, left), instrumented cell (bottom).

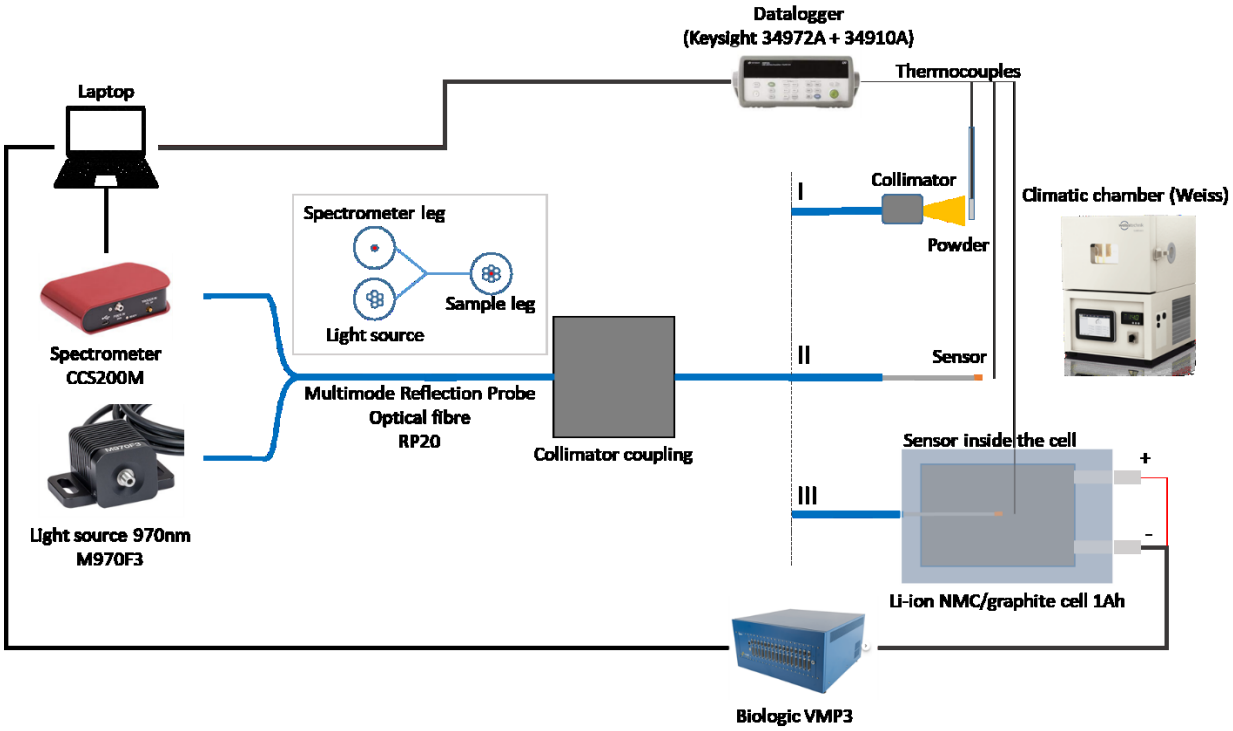

704

705 **Figure S16**: Schematic view of the experimental setup for powder calibration (I), optical fibre
706 sensor calibration (II), calibration and cycling test of the instrumented cell (III).

707

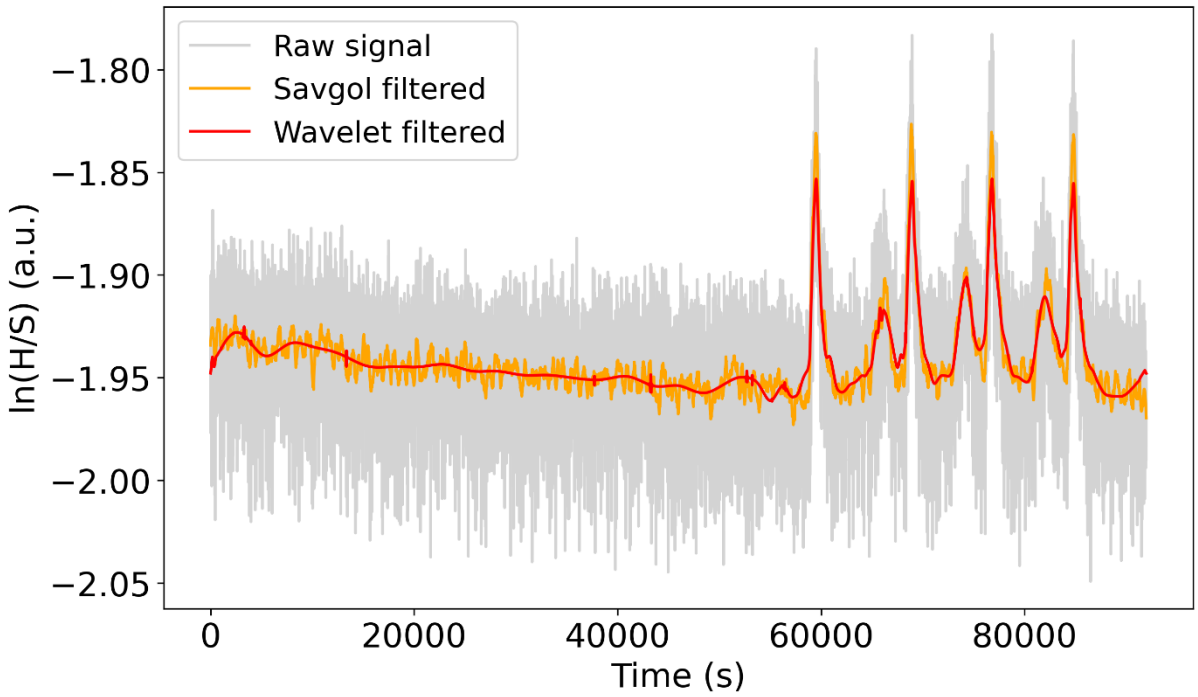

708

709 **Figure S17**: Luminescence signal denoising. Variation of ln(H/S) as a function of time raw signal
710 (gray), savgol filtered (orange), wavelet filtered (red).

711

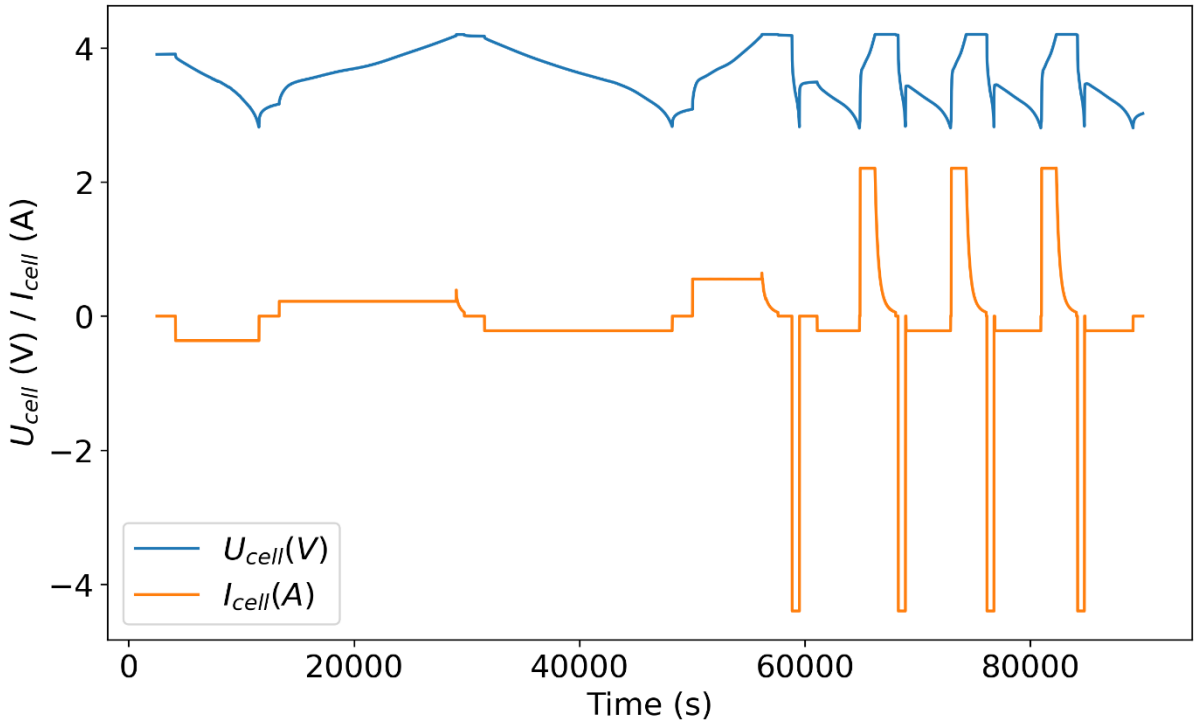

712

713 **Figure S18**: Cycling protocol during the experiment: cell potential (blue), cell current (orange)
714 over time.

715

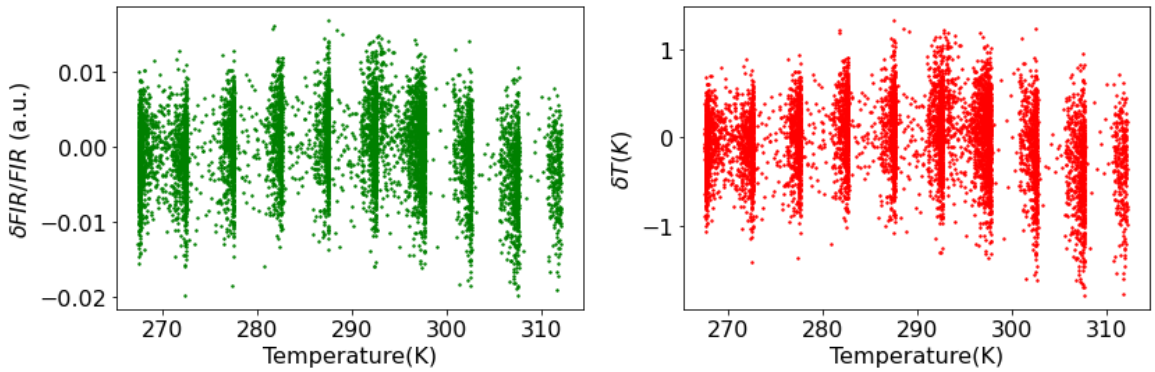

716
717 **Figure S19**: Error δFIR (left) and δT (right) as function of temperature for sensor calculate from
718 calibration curves.

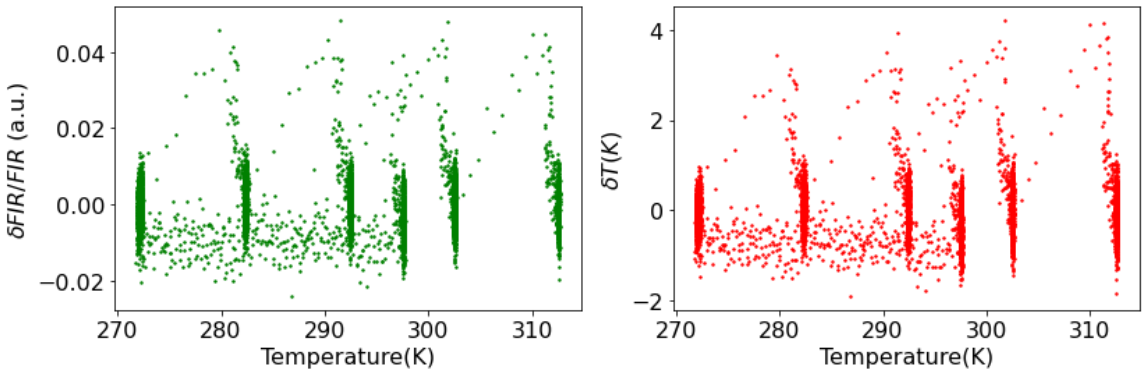

719

720 **Figure S20**: Error δFIR (left) and δT (right) as function of temperature for sensor inside the cell
721 form calibration curves.

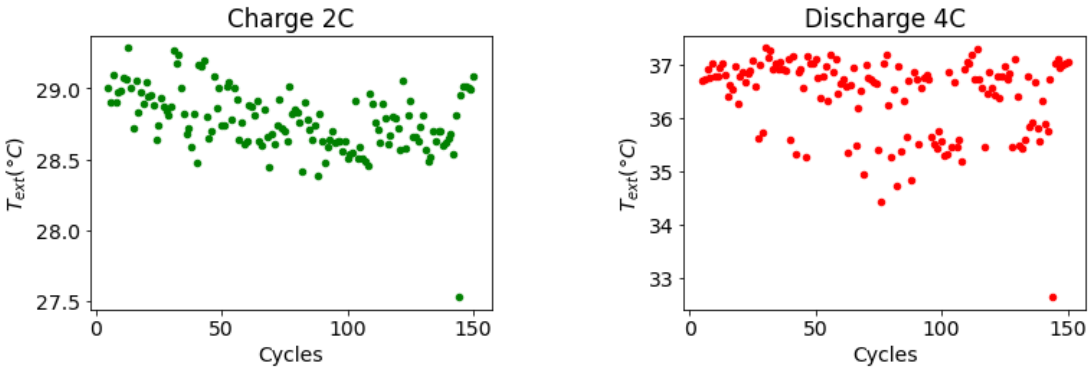

a) b)

722 **Figure S21**: Evolution of the maximum of the external cell temperature T_{ext} during the charge at
723 2C and discharge at 4C over ageing.

724

725

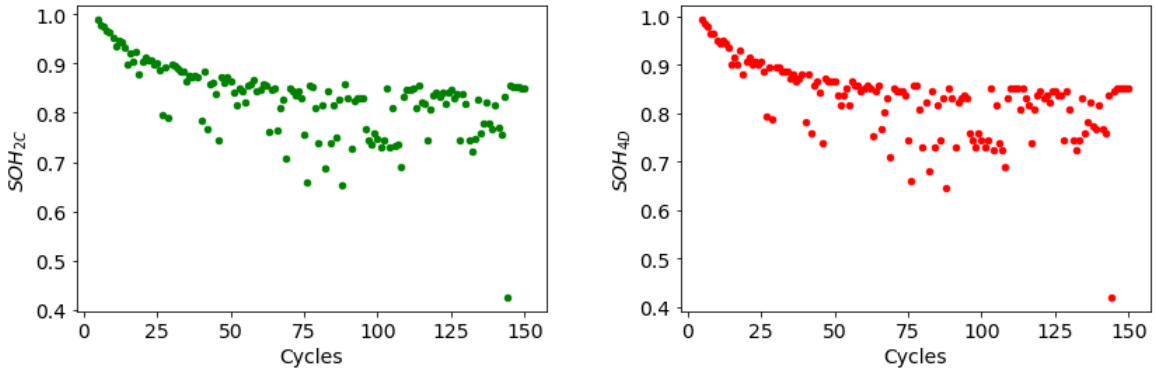

726 **Figure S22**: Evolution of the State of Health (SOH) the charge at 2C and discharge at 4C over
727 ageing.

728

729 **Table S2:** Irreversible capacity (1st Cycle) in % and initial capacity (measured at C/5) in Ah of
730 instrumented and non-instrumented cell

	Irreversible capacity (1st cycle) [%]	Capacity (at C/5) [Ah]
Non instrumented cell	16.4%	1.089
Instrumented cell	16.2%	1.192

731

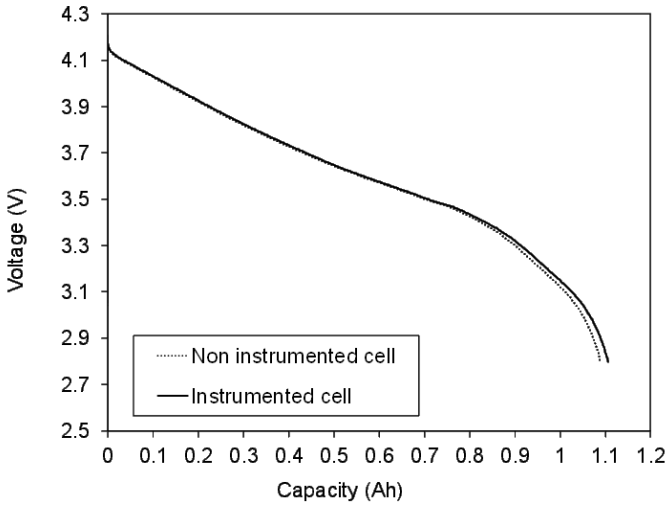

732

733 **Figure S23**: Comparison of cell potential curve of instrumented cell and non-instrumented cell
734 measured at in discharge at C/5 just after formation protocol (initial capacity).

735

736